Mon. Not. R. Astron. Soc. **000**, 1–?? (2010) Printed 24 February 2024 (MN LATEX style file v2.2)

Dynamical Effect of the Turbulence of IGM on the Baryon Fraction Distribution

Weishan Zhu[1,2⋆], Long-Long Feng[1], Li-Zhi Fang[2]
[1]*Purple Mountain Observatory, Nanjing, 210008, China*
[2]*Department of Physics, University of Arizona, Tucson, AZ 85721*

24 February 2024

ABSTRACT

We investigate the dynamical effect of the turbulence in baryonic intergalactic medium (IGM) on the baryon fraction distribution. In the fully developed nonlinear regime, the IGM will evolve into the state of turbulence, containing strong and curved shocks, vorticity and complex structures. Turbulence would lead to the density and velocity fields of the IGM to be different from those of underlying collisionless dark matter. Consequently, the baryon fraction f_b will deviate from its cosmic mean $f_b^{\rm cosmic}$. We study these phenomena with simulation samples produced by the weighted essentially non-oscillatory (WENO) hybrid cosmological hydrodynamic/N-body code, which is effective of capturing shocks and complex structures. We find that the distribution of baryon fraction is highly nonuniform on scales from hundreds kpc to a few of Mpc, and f_b varies from as low as 1% to a few times of the cosmic mean. We further show that the turbulence pressure in the IGM is weakly scale-dependent and comparable to the gravitational energy density of halos with mass around 10^{11} h^{-1} M$_\odot$. The baryon fraction in halos with mass equal to or smaller than 10^{11} h^{-1} M$_\odot$ should be substantially lower than $f_b^{\rm cosmic}$. Numerical results show that f_b is decreasing from $0.8f_b^{\rm cosmic}$ at halo mass scales around 10^{12} h^{-1} M$_\odot$ to $0.3f_b^{\rm cosmic}$ at 10^{11} h^{-1} M$_\odot$ and shows further decrease when halo mass is less than 10^{11} h^{-1} M$_\odot$. The strong mass dependence of f_b is similar to the observed results. Although the simulated f_b in halos are higher than the observed value by a factor of 2, the turbulence of the IGM should be an important dynamical reason leading to the remarkable missing of baryonic matter in halos with mass $\leq 10^{12}$ h^{-1} M$_\odot$.

Key words: cosmology: theory - intergalactic medium - large-scale structure of the universe - methods: numerical

1 INTRODUCTION

In the concordance ΛCDM universe, the baryonic gas (IGM) traces the collisionless cold dark matter in the linear regime of gravitational clustering. However, observation shows that these two components do not related to each other by a linear mapping on scales up to a few Mpc. Most attention on the reason of the IGM-cold dark matter separation on such scales has been drawn to the thermal property of baryonic gas, mainly radiative heating and cooling, such as photo-heating, feedbacks from star formation and accretion to black holes (e.g., Valageas & Silk 1999; Tozzi & Norman 2001; Voit et al. 2002; Zhang & Pen 2003; Xue & Wu 2003).

The hydrodynamical origin of the IGM-dark matter separation has been noticed in the early studies of large scale structure formation (Shandarin & Zel'dovich 1989). Successive studies found that in the weak and moderate nonlinear regime of clustering, the evolution of collisionless particle can be described by the Zel'dovich approximation, while the dynamics of baryonic component is sketched by the adhesion approximation with dissipation of kinetic energy, or by a random force driving Burgers equation (Gurbatov, Saichev, & Shandarin 1989; Berera & Fang 1994; Vergassola et al. 1994; Jones 1999; Matarrese & Mohayaee 2002; Pando, Feng, & Fang 2004). When the Reynolds number is large, Burgers fluid will be turbulent, consisting of shocks (Lässig 2000). Burgers shocks occur not only in high, but also in middle and even low density regions. These shocks could contribute partly to the deviation of the velocity and density fields of the IGM from that of cold dark matter (Pando et al 2004; Kim et al 2005).

A new progress shows that in the highly developed nonlinear regime the velocity field of the IGM is no longer potential, but dominated by vorticity on scales from one and a half hundred kpc to a couple of Mpc (Zhu, Feng & Fang 2010). Oblique shocks will form in inhomogeneous baryonic fluid and act as the source of vorticity of the IGM. These results give supports to the scenario that in the nonlinear regime the baryonic fluid is in the state of fully developed turbulence, which can be characterized by the She-Leveque'

⋆ wszhu@pmo.ac.cn

(SL) scaling (He et al. 2006) and the log-Poisson hierarchy (Liu & Fang 2008). Although tiny vorticity can also be generated in dark matter field during shell crossing, the velocity field of dark matter is still dominated by potential motion on scales around 1 Mpc (Pichon & Bernardeau 1999; Pueblas & Scoccimarro 2008). Consequently, the velocity and density fields of the IGM would depart from those of underlying collisionless dark matter on scales below a few Mpc. Some features predicted from the fully developed turbulence have been found to be consistent with observation, such as the log-Poisson non-Gaussianity of Lyα transmitted flux of quasar's absorption spectrum (Lu , Chu, & Fang 2009; Lu et al. 2010), the scaling relations among the X-ray luminosity, temperature and SZ effect of clusters (Zhang et al 2006; Yuan et al. 2009) and the turbulence broadening of HI and HeII Lyα absorption lines (Zheng et al. 2004; Liu et al. 2006).

In this paper, we extend these studies to the baryon fraction f_b, which is defined as the mass ratio between the baryonic and total matter in a system. In the concordance ΛCDM universe, the cosmic mean of baryon fraction is $f_b^{\rm cosmic} = \Omega_b/\Omega_m = 0.17 \pm 0.01$, where Ω_b and Ω_m are the mean mass density parameters of the baryonic matter and total matter respectively (Dunkley et al. 2009; Komatsu et al. 2009). The baryon fraction in gravitational bound objects is found to be lower than the cosmic mean, known as the missing baryon problem. For galaxy clusters and groups, the baryon fraction is smaller than the cosmic mean by a factor of 2 - 4 (Ettori 2003; Giodini et al. 2009; Dai et al. 2010), while can be as low as about 1% of the cosmic mean for dwarf galaxies(McGaugh et al. 2010). Generally, the baryon fraction decreases monotonically with decreasing mass of collapsed halos. This problem has also been seen in the study of galaxies abundance. The ΛCDM model predicts too many low mass dark matter halos in comparison with estimation from the observed luminosity function of galaxies. It implies that the star formation rate in low mass dark matter halos is substantially low. The baryon content residing in virialized objects with small mass should be much less than that given by the cosmic mean. Additional physics are needed to keep the baryonic matter from overcooling (White & Frenk 1991).

Many kinds of mechanisms have been proposed to prevent most of the baryon falling into dark matter halos. Feedback from supernovae and AGN and photo-heating are well investigated. Feedback from massive stars and SNe were once believed to be able to driving out the collapsed gaseous baryon and hence suppress the star formation(Dekel & Silk 1986; White & Frenk 1991; Kauffmann et al. 1999). Theoretically, simulations and observations have shown that this mechanism is unlike to work while taking appropriate feedback efficiency, mass loss rate(e.g. Mac Low & Ferrara 1999; Benson et al. 2003), except for low mass halos.

In contrast, mechanisms in which the missing baryon are inhibited to fall into the protogalactic halos in the very beginning, i.e., never fell into, are much preferred (Mo et al. 2005; Anderson & Bregman 2010). Photo-heating fulfills this category which adopt a photo-ionizing field to reheat the baryon around progalactic halos and hence keep them from collapse into potential wells(e.g. Efstathiou 1992; Gnedin 2000; Benson 2002). The efficiency of this model, however, was later found to be largely limited, only works for halos below 10^{10} M$\odot$ (Hoeft et al. 2006), because the central self-shielding will delay the photo-evaporation.

In our view, IGM turbulence should be an important reason of the missing baryon problem. The effects of turbulence on the properties of clusters have been extensively studied by numerical simulations and theoretical works(e.g. Norman & Bryan 1999; Dolag et al. 2005; Vazza et al. 2009, 2010; Burns, Skillman& O'Shea 2010; Ruszkowski & Oh 2010). Yet, we will focus on the dynamical and statistical effect of turbulence on the spatial distribution of baryon fraction. That is, the turbulence of IGM is treated as a basic environment factor of gravitational clustering. The baryon missing in virialized objects should be a result of the formation and evolution of inhomogeneity of f_b spatial distribution. One can then explain the baryon missing by considering the inhibition of gravitational collapse by turbulence pressure (Chandrasekhar 1951a, 1951b).

This paper is organized as follows. §2 addresses the theoretic background of turbulence in the IGM and its effect on the gravitational collapsing of baryonic matter. §3 gives the simulation method of producing samples. In §4, we study the properties of the non-uniform distribution of the baryon fraction, and its relation with turbulence. §5 presents the baryon fraction in collapsed halos. We discuss our results and compare them with previous numerical studies in §6. Finally, the conclusions are given in §7.

2 THEORETICAL BACKGROUND

2.1 Turbulent IGM

Hierarchical structure formation process will introduce shocks(Ryu et al. 2003; Pfrommer et al. 2006; Vazza et al. 2009). The shock wakes and shear flows, arose from gas accreting into pancakes, filaments and halos, protogalactic and collapsed objects moving in complex structures and gaseous structure colliding and merging, will interplay with each other and drive instability, result in the onset of turbulence. Fully developed turbulence consists of eddies on various scales and will cascade the kinetic energy of largest eddies down to smaller one (Lin 1966; Shu 1992).

More specifically, the evolution of baryonic fluid in the moderate nonlinear regime can be characterized by random force driving Burgers equation (Gurbatov et al. 1989; Berera & Fang, 1994; Jones, 1999; Matarrese & Mohayaee, 2002). When the effective Reynolds number is large, burgers fluid will be turbulent, consisting of shocks and complex structures on various scales(Polyakov, 1995; Lässig 2000; Boldyrev et al. 2004). As dark matter is not influenced by Burgers turbulence, the IGM velocity field will dynamically decouple from the dark matter field on scales larger than the Jeans length once Burgers turbulence is developed. This will lead to the deviation of f_b from $f_b^{\rm cosmic}$ in low and high density areas.

The velocity field of baryonic fluid keeps irrotational in the moderate nonlinear regime. Latter on, the velocity field of IGM will no longer be potential dominated, because the vorticity can be effectively generated by oblique shocks due to baroclinic instability(Zhu et al 2010). When shocks propagate in inhomogeneous medium, they will generally evolve into oblique or curved shock waves (e.g. Landau & Lifshitz 1987), acting as the source of vorticity (e.g. Picone et al. 1984; Emanuel 2000). Once triggered, the vorticity can be self-amplified by the nonlinearity of hydrodynamics (see §2.3). Finally the IGM evolves into a fully developed turbulent state which satisfies the She-Leveque scaling and log-Poisson hierarchy (He et al. 2006; Liu & Fang 2008; Lu et al 2009, 2010). More details about the development of turbulence in the IGM along cosmit evolution can be found in (Zhu et al. 2010; Fang & Zhu 2011).

2.2 Turbulence pressure and vorticity of IGM

The Jeans length of self-gravitational clustering in a statistical uniform gas with density ρ and speed of sound c_s with or without turbulent gas motion has been studied by Chandrasekhar (1951a, 1951b). In the absence of turbulence, the Jeans length is $\lambda_J = c_s\sqrt{\pi/G\rho}$, i.e. gravitational clustering can occur only if the perturbation scale is larger than λ_J. The effect of turbulent motions on the clustering is to replace c_s by an effective sound speed

$$c^2_{\rm s,eff} = c^2_s + \frac{1}{3}\langle v^2\rangle \tag{1}$$

where $\langle v^2\rangle$ measures the velocity fluctuations of turbulence. The Jeans length is increased by the random velocity field of turbulence, which plays the similar role as the randomly thermal motion. The random motion of the turbulence provides an extra pressure, $p_{\rm tub} = \langle\rho v^2\rangle$, called turbulence pressure. The turbulence pressure, joining the thermal pressure, will slow down and even halt the IGM falling into a gravitational well.

Considering the gravitational collapsing on scale R will not be affected by the velocity dispersion on scales that larger than R, the velocity fluctuations with wave-numbers $k < 2\pi/R$ will not resist gravitational collapsing on scales larger than R. Consequently, the effect of turbulence pressure on gravitational collapsing on scale R could be estimated by (Bonazzola et al 1987)

$$p_{\rm tur} = \int_{\max(k_{\rm R},k_{\rm min})}^{k_{\rm max}} E(k)dk, \tag{2}$$

where $E(k)$ is the power spectrum of kinetic energy density $(1/2)\rho(\mathbf{r})v^2(\mathbf{r})$ of the turbulence. The upper limit of the integral eq.(2) $k_{\rm max} = 2\pi/l_{\rm diss}$ corresponds to the minimal scale $l_{\rm diss}$ below which the turbulence is dissipated. The lower limit of the integral eq.(2) is the maximum of $k_{\rm R}$ and $k_{\rm min}$, where $k_{\rm R} = 2\pi/R$ and $k_{\rm min}$ matches the upper scale of turbulence. Obviously, the turbulent pressure $p_{\rm tur}$ is dynamical, not thermal. It can be comparable to the thermal pressure of the IGM, especially in regions the temperature of IGM is not very high.

When we estimate the turbulence pressure with eq.(1) or (2), we should separate the velocity field $\mathbf{v}(\mathbf{r},t)$ into two components: one is the random motion of turbulence and the other is the bulk velocity. The latter mainly depends on the gravitational potential, and does not contribute to the turbulence pressure. In some algorithms, the bulk velocity is identified as the mean velocity within a box, while the fluctuation with respect to the mean velocity is supposed to be the turbulent motion. As the box size is selected by hand, these algorithms might contain non-ignorable system bias. A better way to pick up the random motion of turbulence bases on the vorticity of velocity field.

The vorticity field $\vec{\omega}(\mathbf{r},t)$ of the velocity field $\mathbf{v}$ of the IGM is defined by $\omega_i = (1/2)(\partial_i v_j - \partial_j v_i)$, i.e., $\vec{\omega} = \nabla\times\mathbf{v}$, where $i = 1, 2, 3$. The dynamical equation of the vorticity $\vec{\omega}$ is (Zhu et al. 2010)

$$\begin{aligned}\frac{D\vec{\omega}}{Dt} &\equiv \partial_t\vec{\omega} + \frac{1}{a}\mathbf{v}\cdot\nabla\vec{\omega} \\ &= \frac{1}{a}(\mathbf{S}\cdot\vec{\omega} - d\vec{\omega} + \frac{1}{\rho^2}\nabla\rho\times\nabla p - \dot{a}\vec{\omega}),\end{aligned} \tag{3}$$

where p is the pressure of the IGM, $d = \partial_i v_i$ is the divergence of the velocity field and $a(t)$ is the cosmic factor. Tensor $\mathbf{S}$, defined as $S_{ij} = (1/2)(\partial_i v_j + \partial_j v_i)$, is called strain rate, and $[\mathbf{S}\cdot\vec{\omega}]_i = S_{ij}\omega_j$. A remarkable property of eq.(3) is the absence of the gravity term . This point is expected, as gravity is curl-free in nature. In other words, vorticity is fully given by the nonlinearity of hydrodynamics and hence is effective to measure the turbulence.

An important property of the vorticity is that for a fully developed turbulence the power spectra of the vorticity field $P_\omega(k)$ and the velocity field $P_v(k)$ should satisfy $P_\omega(k) = k^2P_v(\mathbf{r})$ (Batchelor 1959, 2000). This relation can be used to determine the wavenumber $k_{\rm min}$, i.e. the upper scale of fully developed turbulence. We use this criterion to ascertain $k_{\rm min}$ to calculate the integral eq.(2).

2.3 Dynamical effect of turbulence on IGM gravitational clustering

The dynamical effect of turbulence on the gravitational clustering of the IGM can be seen with the time evolution of the irrotational component of velocity field, i.e. the divergence of velocity field $d = \partial_i v_i$, which follows (Zhu et al 2010)

$$\begin{aligned}-\frac{Dd}{Dt} &\equiv -\partial_t d - \frac{1}{a}\mathbf{v}\cdot\nabla d = \\ &= \frac{1}{a}\left[S_{ij}S_{ij} - \frac{1}{2}\omega^2 + \frac{1}{\rho}\nabla^2 p - \frac{1}{\rho^2}(\nabla\rho)\cdot(\nabla p)\right. \\ &\quad \left. + \frac{4\pi G}{a}(\rho_{\rm tot} - \rho_0) + \dot{a}d\right],\end{aligned} \tag{4}$$

where $\rho_{\rm tot}$ is the total mass density including both cold dark and baryonic matter with ρ_0 being its mean value. As negative divergence means the increase of density, positive $4\pi G(\rho_{tot} - \rho_0)/a$ will lead to clustering, while negative one result in anti-clustering. The right hand side of eq.(4) can be used to compare the effects of hydrodynamical terms on clustering with that of gravity.

We first identify the physical meaning of the hydrodynamical terms on the right hand sight of eq.(4) by considering incompressible fluid, i.e. assuming $\rho_{\rm tot}$ to be a constant $\rho_{\rm tot} = \rho_0$. In this case, the term of gravity $(4\pi/a)(\rho_{\rm tot} - \rho_0) = 0$, and $\nabla\rho = 0$. The continuity equation yields $d = 0$, and Eq.(4) gives

$$\nabla^2 p = -\rho\left(S_{ij}S_{ij} - \frac{1}{2}\omega^2\right). \tag{5}$$

This is a typical Poisson equation for the scalar field p. Analogous to the field equations in electrostatics, the term $\rho[S_{ij}S_{ij} - 1/2\omega^2]$ on the right hand side of eq.(5) plays the role of the "charge" of a pressure field. Positive "charge" produces an attraction force, while negative "charge" yields a repulsive force. Back to eq.(4), $\rho[S_{ij}S_{ij} - 1/2\omega^2]$ also plays the role of nonthermal pressure of turbulence. In regions with negative "charge", i.e. $[S_{ij}S_{ij} - (1/2)\omega^2] < 0$, the turbulent fluid will prevent the gravitational clustering.

The sign of the "charge" is actually determined by the levels that turbulence has developed. From the definition of vorticity and strain rate, we have

$$\frac{1}{2}\omega^2 - S_{ij}S_{ij} = \frac{1}{2}[(\partial_i v_j)(\partial_i v_j) - 3(\partial_j v_i)(\partial_i v_j)]. \tag{6}$$

For a Gaussian velocity field, $\langle 3(\partial_j v_i)(\partial_i v_j)\rangle = \langle(\partial_i v_j)(\partial_i v_j)\rangle$, the net effect of velocity fluctuations on the IGM collapsing is null in average. However, for a non-Gaussian velocity field, it can be either positive or negative, depending on the property of the velocity field. For a homogeneous and isotropic turbulence , $\langle(\partial_i v_j)(\partial_j v_i)\rangle = 0$ (Batchelor 1959), the sign of the "charge", $\rho[S_{ij}S_{ij} - 1/2\omega^2]$, is always negative. A fully developed turbulent flow will generally prevent the IGM from gravitational collapsing.

The term $\nabla^2 p/\rho$ of eq.(4) relates to the hydrostatic pressure while does not consider fluid compressibility, which has been presented in eq.(5). It is mostly negative in overdense collapsing regions, and will resist upon gravitational collapse. The term $-(\nabla\rho)\cdot(\nabla p)/\rho^2$ on the right hand side of eq.(4) result from the compressibility of the IGM. Its value would be negative when the density-pressure relation is a power law $p \propto \rho^\gamma$ and $\gamma > 0$, and then also plays the role of resisting gravitational collapsing.

The physical meaning of the term $(\nabla\rho)\cdot(\nabla p)/\rho^2$ can be shown by the ratio between $(\nabla\rho)\cdot(\nabla p)/\rho^2$ and the gravity term $4\pi G(\rho_{\rm tot}-\rho_0)$. The ratio is roughly equal to $\sim (t_{\rm infall}/t_{\rm sound})^2$, where $t_{\rm infall} \sim (G\rho)^{1/2}$ is the free falling time scale, $t_{\rm sound} \sim R/c_s$, $c_s \sim (\nabla p/\nabla\rho)^{1/2}$, is the dynamical time scale on a spatial scale R collapsing. When $(t_{\rm infall}/t_{\rm sound})^2$ is larger than 1.0, the free falling time scale is larger than the dynamical time scale, and in result, the collapsing on scale R is significantly prevented.

3 METHOD

As mentioned above, the turbulent IGM contains curved shocks, vortices, and other discontinuities. To study the effect of turbulent IGM with simulation, the algorithm should be qualify for capturing these complex structures. We take advantage of the development of the Weighted Essentially Non-oscillatory (WENO) method (Shu 1999). The WENO schemes have been widely used in various fields, such as high Reynolds number compressible flows (Zhang et al. 2003), high Mach number jets (Carrillo et al. 2003), magneto-hydrodynamics (Jiang & Wu, 1999) and hypersonic boundary layer (Rehman et al 2009). The shock capturing algorithm with WENO scheme has past many test, including shock-boundary layer interaction (Lagha et al. 2009), shocks in high-speed flows (Martin, Piomelli & Candler 2000), shock vortex interaction (Grasso & Pirzzoli 2000a, 2000b) and shock-turbulence interaction (Pirozzoll 2002). An updated review of the WENO method is given in Shu 2009.

In the context of cosmological hydrodynamical simulation, the WIGEON code is based on Eulerian description of hydrodynamics with 5th order WENO finite difference scheme and particle mesh (PM) method for dark matter particles (Feng, Shu, & Zhang 2004). The WIGEON code can reproduce commonly accepted results such as the relation between IGM temperature and density and the component of WHIM (He, Feng, & Fang 2004). In the same time, it also reveals a series of turbulent behavior of the IGM (He at al 2006; Liu & Fang 2008; Lu et al. 2009, 2010). These features of this code fit well with our goal.

The cosmological parameters are taken to be $(\Omega_m, \Omega_\Lambda, h, \sigma_8, \Omega_b, n_s, z_{re}) = (0.274,\ 0.726,\ 0.705,\ 0.812,\ 0.0456,\ 0.96,\ 11.0)$ (Komatsu et al., 2009). The simulation run in a periodic cubic box of size 25 h^{-1} Mpc since redshift $z = 99$ with a 512^3 grid and an equal number of dark matter particles, giving a mass resolution of $1.04\times10^7 M_\odot$. A uniform UV background of ionizing photons is added at $z_{\rm re}$ to mimic the reionization. Radiative cooling and heating are followed as Theuns et al. (1998) with the primordial composition $X = 0.76, Y = 0.24$. Star formation and its feedback are not added in our simulation, because the resolution we used makes it hard to implant these processes appropriately. Snapshots are outputted at redshifts $z = 11.0, 6.0, 4.0, 3.0, 2.0, 1.0, 0.5, 0.0$. To study the convergence of numerical results, we also run a simulation with 256^3 grid and an equal number of dark matter particles.

The velocity field of simulation samples has been used to show the development of vorticity and turbulence in Zhu et al.(2010). To locate shocks post simulation we use a algorithm also based on WENO kernel, combining with conditions from Ryu et al.(2003) (see Appendix). To construct the density field of dark matter on grids, we assign the mass of dark matter particles onto grids using the Triangle-Shaped-Cloud (TSC) method. In order to minimize the system bias of assignment in calculating the baryon fraction on grids, we smooth over the density fields of baryonic and dark matter on grids separately using the same smooth window with radius of one grid.

To identify halos of dark matter and their radius r_{200}, we use the same process as Crain et al. (2007). Halos are identified by two methods: a.) friends-of-friends (FOF) method with a linking length parameter 0.2; b.) HOP method (Eisenstein & Hut 1998) with default parameters for group searching and $\delta_{\rm outer} = 80$, $\delta_{\rm saddle} = 200$ and $\delta_{\rm peak} = 240$ for group merging. We study only halos consisting of no less than 2000 dark matter particles at $z = 0$. For each halo, we can then find the center and radius of a sphere, in which the mean mass density is equal to $200\rho_{\rm crit}(z)$, where $\rho_{\rm crit}(z) = 3H^2(z)/8\pi G$ is the critical density at redshift z.

4 SPATIAL DISTRIBUTION OF BARYON FRACTION

4.1 A Slice

Figure 1 presents an example of the spatial distributions of baryonic and dark matter density in a slice of 25x25x0.2 h^{-3} Mpc^3 at redshift $z = 0$. The density fields of dark matter and baryonic fluid of Figure 1 display the typical sheets-filaments-knot structures on the cosmic scales.

The spatial distributions of shock, temperature, vorticity and normalized baryon fraction $F_b \equiv f_b/f_b^{\rm cosmic}$ on the same slice are shown in Figure 2. The shocks do not always follow the filament and sheet structures of the matter density fields. Shocks can also be formed in low density areas, as demonstrated in other simulations (e.g. Ryu et al. 2003; Kang et al. 2007).

The vorticity field in Figure 2 is described by the dimensionless quantity ωt, where t is the cosmic time. ωt accounts the number of rotation of the vorticity ω in the age of universe. The distribution of vorticity also doesn't always follow the filament and sheet structures of the matter density fields, but has cloud-like structures (Zhu et al 2010).

Although curved shocks are the sources of vorticity, the spatial distribution of vorticity field does not show the same configuration as the shocks. It is because the spatial transfer of vorticity is given by the velocity field [eq.(3)], while the case with shock front is different. Once the vorticity appears, it will depart from their source-curved shocks and spreads over the space along with the velocity field (Batchelor 2000).

In the plot of vorticity distribution, we add FOF identified halos, which are marked as solid circles. The radius of circles are enlarged to 5 times of the real halos radius. A remarkable feature is that all the halos are located in the area of $\lg\omega t \geq 1$. It means that all the gravitational bounded halos are formed in the environment of turbulent IGM. As discussed in §2.2, the gravitational clustering should be affected by the turbulence pressure.

The spatial distribution of the normalized baryon fraction F_b is highly non-uniform. The value of F_b spreads over three orders of magnitude from $\lg F_b \sim -2$ to ~ 1, indicating that the separation of baryonic matter from dark matter is significant developed during the nonlinear evolution. The deviation of baryon fraction from

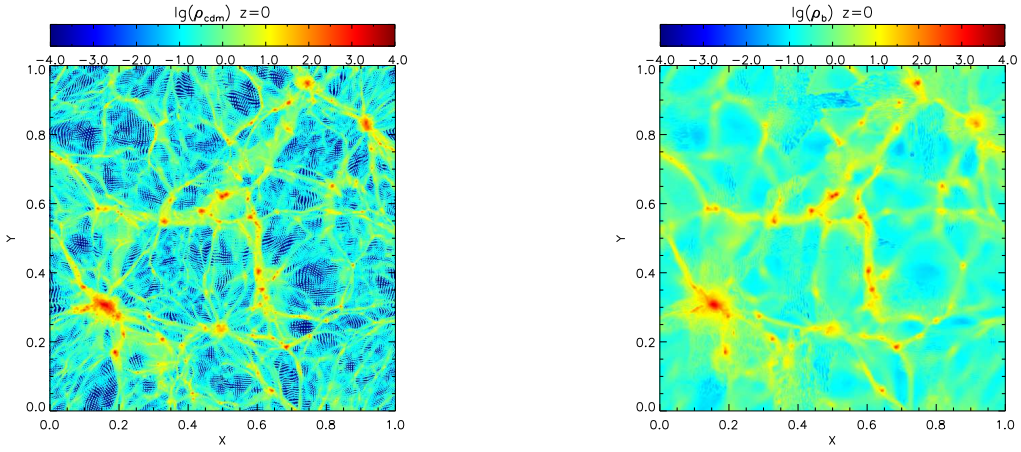

Figure 1. Distributions of dark matter density (left); baryon density (right) in a slice of 25x25x0.2 h^{-3} Mpc^3 at redshift $z = 0$.

the cosmic mean is not only occurred in or around massive halos, but also in the low and moderate density areas. The spatial distribution of baryon fraction does not display the sheets-filaments-knot structures as the density fields of dark and baryonic matter do. Nevertheless, the area of high $\rho_{\rm cdm}$ are surrounded by high baryon fraction area (dark blue), indicating that the processes of separating baryonic matter from dark matter would be potent around high density areas. The sizes of some region in which $\lg F_b \leq -0.5$, corresponding to $F_b \leq 0.3$, is much larger than the resolution, demonstrating that the existence of regions with $F_b \leq 0.3$ is robust.

4.2 Comparing the effects of turbulence and gravity on clustering

As mentioned in §2.3, the term $(4\pi G/a)(\rho_{\rm tot} - \rho_0)$ on the right hand side of eq.(4) measures the gravity effect leading to clustering ($\rho_{\rm tot} > \rho_0$), or anti-clustering ($\rho_{\rm tot} < \rho_0$). The first three terms on the right hand side of eq.(4) describe the gas dynamical and thermal effects, namely, the vorticity and strain rate $-\omega^2/2 + S_{ij}S_{ij}$, the ordinary pressure $\nabla^2 p/\rho$ and multiphase-related term $-(\nabla\rho)\cdot(\nabla p)/\rho^2$. We now use simulation sample to study the general properties of these terms.

Figure 3 presents a comparison between $(\nabla\rho)\cdot(\nabla p)/\rho^2$ and $4\pi G(\rho_{\rm tot} - \rho_0)$ in cells randomly selected from the simulation samples at $z = 0$. We chose only the cells of $4\pi G(\rho_{\rm tot} - \rho_0) > 0$, which drives collapsing. The variables used in Fig. 3, $(1/\rho^2)(\nabla\rho)\cdot(\nabla p)t^2$ and $4\pi G(\rho_{\rm tot} - \rho_0)t^2$, are dimensionless, where t is the age of the universe.

We can see from Figure 3, when $4\pi G(\rho_{\rm tot} - \rho_0) < 50$, more than a half of the data points having $(\nabla\rho)\cdot(\nabla p)/\rho^2 > 4\pi G(\rho_{\rm tot} - \rho_0)$ and few points have $(\nabla\rho)\cdot(\nabla p)/\rho^2 < 0$, which corresponds to the so-called inverse density-pressure(temperature) relation. Therefore, the term $(\nabla\rho)\cdot(\nabla p)/\rho^2$ enhanced by shocks and complex structures can effectively resist gravitational collapsing till $4\pi G(\rho_{\rm tot} - \rho_0) \sim 50$. For deep gravity wells with $4\pi G(\rho_{\rm tot} - \rho_0) > 50$, most data points show that gravity generally is larger than $(\nabla\rho)\cdot(\nabla p)/\rho^2$. Namely, only in deep gravitational wells the motion of baryonic matter will be dominated by the gravity.

Figure 4 compares $\omega^2/2 - S_{ij}S_{ij}$ vs. $(\nabla\rho)\cdot(\nabla p)/\rho^2$ (left panel), and $(1/2)\omega^2 - S_{ij}S_{ij}$ vs. $(1/\rho)\nabla^2 p$ (right panel) at randomly selected cells. We use the dimensionless variables by multiplying with t^2. The left panel of Figure 4 shows that the magnitude of $\omega^2/2 - S_{ij}S_{ij}$ is comparable with $(\nabla\rho)\cdot(\nabla p)/\rho^2$. While in the right panel, it exhibits that term $(1/2)\omega^2 - S_{ij}S_{ij}$ is stronger than the term $(1/\rho)\nabla^2 p$. On average, the term $(1/\rho)\nabla^2 p$ is smaller than $(\nabla\rho)\cdot(\nabla p)/\rho^2$.

In a word, in terms of prevention of gravitational collapsing, the effect of vorticity and strain rate is comparable with $(\nabla\rho)\cdot(\nabla p)/\rho^2$ and dominates over $(1/\rho)\nabla^2 p$. Both of the latter two terms are thermal pressure p related, one can regard vorticity and strain rate as an effective thermal pressure. Figure 2 shows that in most regions IGM temperature are equal to or less than 10^6 K. Giving the comparison in the last paragraph, the effective thermal pressure of turbulence would be as strong as the thermal pressure with temperature $\sim 10^{5-6}$ K. The turbulence pressure level given by simplified estimation is consistent with the more delicate one using the energy density of turbulence in Zhu et al. (2010).

4.3 Correlations between baryon fraction and turbulence

As vorticity is an important dynamical factor to cause a low baryon fraction, one can expect a correlation between the baryon fraction and the vorticity. Figure 5 gives the probability density function(PDF) of $\lg[(\omega t)^2/2]$ in various ranges of the baryon fraction F_b. Figure 5 indeed shows that for cells have small F_b, the PDF at the side of $\lg[(\omega t)^2/2] > 2$ are higher. The cells with more serious baryon missing have larger vorticities in average.

The similar PDF of $\lg|(1/\rho)(\nabla^2 p)t^2|$ is also shown in Figure 5. The cells with more significant baron missing generally corresponds to large $|(1/\rho)(\nabla^2 p)t^2|$ as well. Although the two panels of Figure 5 look similar, the values of $(\omega t)^2/2t^2$ and $|(1/\rho)(\nabla^2 p)t^2|$ actually cover different magnitude range. The former can be as large as 10^6, while the later is about 10^5. This is consistent with the right panel of Figure 4. The vorticity term $(\omega t)^2/2$ is larger than the term $(1/\rho)(\nabla^2 p)t^2$.

Figure 6 plots the F_b vs. mass density of dark matter in randomly selected cells in which $(1/2)\omega^2 - S_{ij}S_{ij}$ is positive and $(1/2)\omega^2 - S_{ij}S_{ij}$ dominant over $|4\pi G(\rho_{\rm tot} - \rho_0)|$. It shows clearly that the higher the density $\rho_{\rm cdm}$ the lower the baryon fraction F_b. Since high density $\rho_{\rm cdm}$ means high $|4\pi G(\rho_{\rm tot} - \rho_0)|$, Figure 6 indicates that as long as the turbulence of the IGM is dominant, the baryon fraction is lower for higher $\rho_{\rm cdm}$.

We can also see from Figure 6 that a significant fraction of those data point which have $F_b \leq 0.3$, i.e. more than 70 percent of

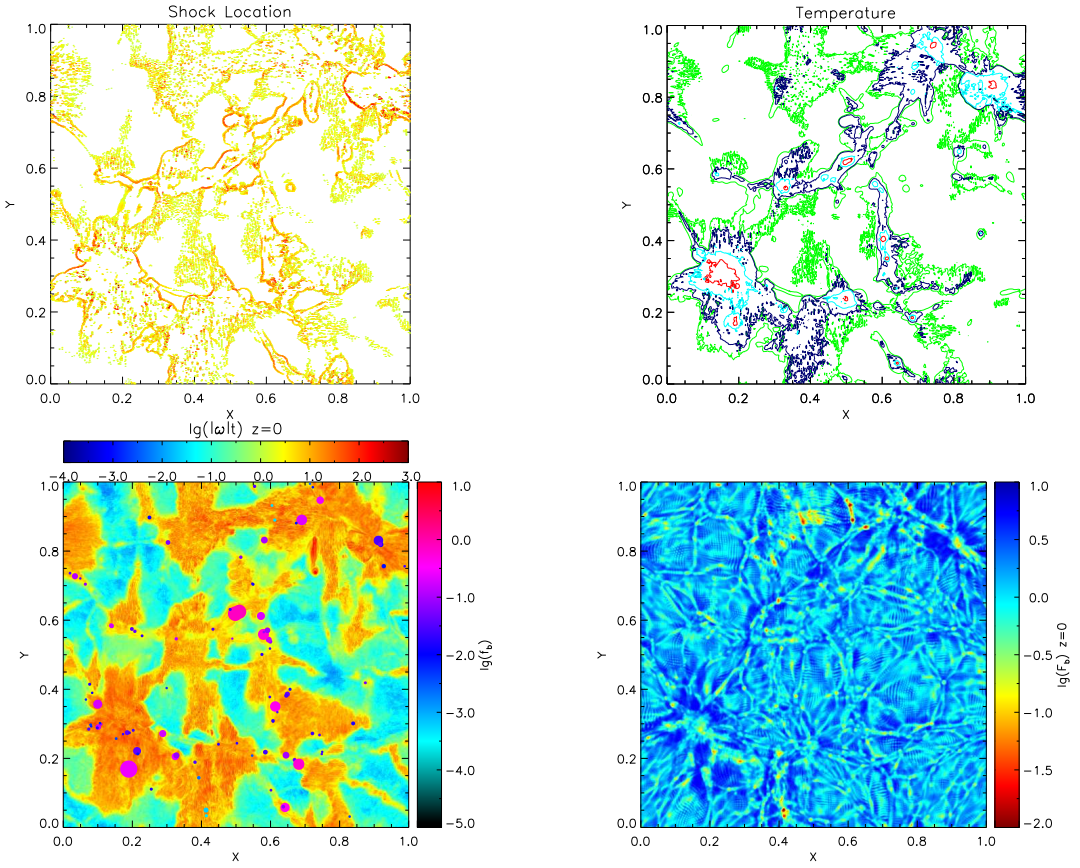

Figure 2. The top left shows shocks with Mach number $M_a \sim 1-10$ (green), $\sim 10-100$ (yellow) and > 100 (red). The top right is the temperature contours with green, navy, cyan and red representing 10^4, 10^5, 10^6, 10^7 K, respectively. The bottom left is the vorticity in the slice, in which the solid circles are halos identified by FOF method. The radius of each solid circle is equal to 5 times of the halo radius. The bottom right is the normalized baron fraction $F_b = f_b/f_b^{\rm cosmic}$.

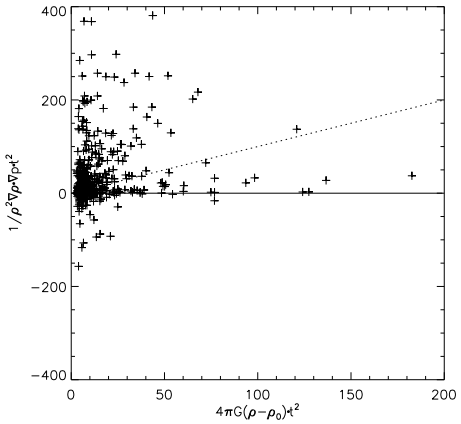

Figure 3. $(\nabla\rho)\cdot(\nabla p)/\rho^2$ vs. $4\pi G(\rho_{tot}-\rho_0)$ of randomly selected cells at $z=0$. The dotted line shows $(\nabla\rho)\cdot(\nabla p)/\rho^2 = 4\pi G(\rho_{tot}-\rho_0)$.

baryonic matter are missing, locate in the areas with mass density $\rho_{\rm cmd} \sim 1$. The event of $F_b \leq 0.3$ baryon missing can occur even in the regions out of collapsed clumps, indicating that the baryon missing of virialized halos should be considered as result of the evolution of baryon distribution on sizes larger than virialized halos.

5 BARYON FRACTION OF DARK MATTER HALOS

5.1 Turbulence pressure and halo mass

It has been shown that the relation $P_\omega(k) = k^2 P_v(\mathbf{r})$ is well satisfied by the IGM velocity field in the scale range from 0.2 to 3 h^{-1} Mpc at $z = 0$ (Zhu et al 2010), on which the IGM is in the state of fully developed homogeneous and isotropic turbulence. The power spectrum of kinetic energy density of the turbulence is ap-

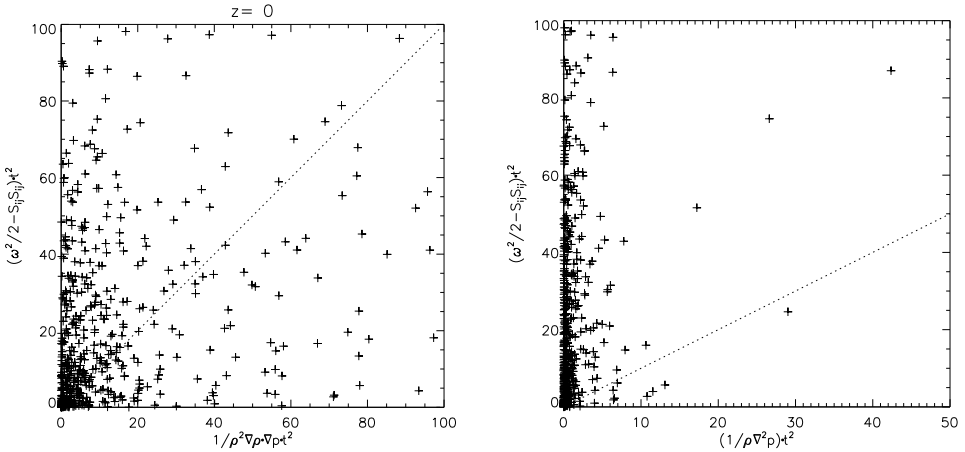

Figure 4. Left panel: $(1/2)\omega^2 - S_{ij}S_{ij}$ vs. $(\nabla\rho)\cdot(\nabla p)/\rho^2$ in randomly selected cells at redshift $z = 0$. Right panel: $(1/2)\omega^2 - S_{ij}S_{ij}$ vs. $(1/\rho)\nabla^2 p$ of the same cells.

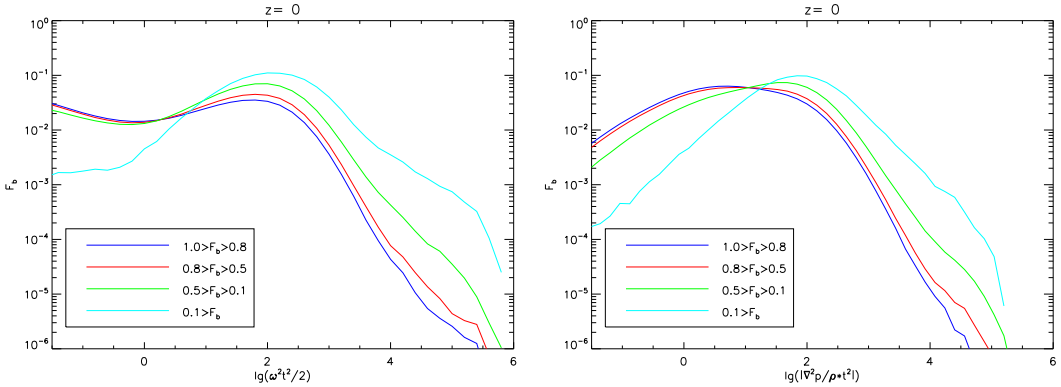

Figure 5. The PDF of $\lg|\omega^2 t^2|$ (left) and $\lg|\nabla^2 p/\rho t^2|$ (right) for four ranges of F_b: a.) $0.8 - 1.0$ (blue); b.) $0.5 - 0.8$ (red); c.) $0.1 - 0.5$ (green), and d.) < 0.1 (cyan) for sample at redshift $z = 0$.

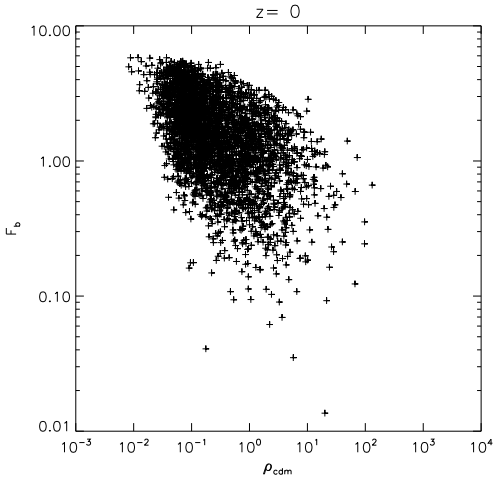

Figure 6. F_b vs. mass density of CDM, in unit of cosmic mean, of cells randomly selected from those in which $(1/2)\omega^2 - S_{ij}S_{ij}$ is positive and $(1/2)\omega^2 - S_{ij}S_{ij} > |4\pi G(\rho_{tot} - \rho_0)|$.

proximately $E(k) \propto k^{-1.4}$. The turbulence pressure (or the kinetic energy density) is weakly scale-dependent $p_{\rm tur}(R) \propto R^{-0.4}$ and about the order of magnitude $\sim 1 \times 10^{-16}$ g cm^{-1} s^{-2}. On the other hand, the viral temperature T_{200} of a halo at the virial radius r_{200} is $\propto r_{200}^2$. The kinetic energy density of the virial motion at r_{200} is then $\sim 1 \times 10^{-16}(T_{200}/10^{5.5})$. The mass of halos with $T_{200} = 10^{5.5}$ K is about $10^{11}\ h^{-1}\ M_\odot$. Obviously, the effect of turbulence pressure on the IGM collapsing would be comparable with and even larger than the gravity for halos with mass equal to and less than $10^{11}\ h^{-1}\ M_\odot$. The baryon fraction would significantly be reduced for halos with mass $\leq 10^{11}\ h^{-1}\ M_\odot$.

Meanwhile, the kinetic energy density of turbulence is small than that of the virial motion of halos with mass larger than times of $10^{11}\ h^{-1}\ M_\odot$. Thus, the halo mass dependence of the baryon massing would show two phases: when the halo mass is larger than times of $10^{11}\ h^{-1}\ M_\odot$, the baryon fraction f_b is not much affected by turbulent IGM, and it will be substantially decreasing with halo mass when halo mass is lower than a few $10^{11}\ h^{-1}\ M_\odot$.

5.2 Halo mass dependence of baryon fraction

With the preparation of above sections, we now analysis the baryon fraction in gravitational collapsed halos. The accuracy of the baryon fraction in selected halos relies on the calculation of the mass of baryonic matter enclosed in the viral radius. To reduce the system error, we divide each halo sphere into sub-cubic cells with size equal to $1/50$ of the sphere radius. We then use Cloud-In-Cell (CIC) interpolation to determine the baryon density at each sub-cell. The halo mass M_{200} and baryon mass are given by the sum of the mass of total matter and baryonic matter respectively in all the sub-cubic cells. This method may yield large uncertainty for halos with r_{200} less than the size of a grid. To restrain the uncertainty, our statistical results mainly are on $M_{200} \geq 10^{11} M_\odot$, i.e. the virial radius is about equal to or larger than two grids.

Figure 7 displays the baryon fraction as a function of halo mass at $z = 0$, where the halos are identified by FOF (left) and HOP (right) respectively. The results of the two panels are statistically the identical. At a given halo mass, there are large scatters in the baryon fraction F_b, the scatters are seen to be even more significant in the FOF algorithm than the HOP. This is consistent with Figures 6, which indicates a large scatter in F_b at a given mass density. The distribution of F_b is highly non-Gaussian and has a long tail on the side of small F_b, conforming with statistics of turbulent fluid, of which the velocity and density fields are intermittent and their PDFs have long tails.

Regardless of the scatters, the distribution of F_b in Figure 7 can not be described by a single power law, but shows two distinct phases in halo mass-dependence. In the mass range $10^{12} - 10^{13}$ $h^{-1}\ M_\odot$, F_b is weakly dependent on halo mass and takes a value of 80% to 90% of the cosmic mean, which is the first phase. When halo mass is less than $\leq 10^{12}\ M_\odot$, F_b is quickly dropping off with decreasing halo mass, i.e. the second phase. At mass$\sim 10^{11}$ $h^{-1}\ M_\odot$, F_b is around 0.3 of the cosmic mean. For halos with mass $M_{200} = 3 \times 10^{10} M_\odot$, the mean of F_b is even as low as about 0.1. Although the data points in the second phase shows a large scattering, this phase has a clear upper envelop. The strong downward in F_b with decreasing halo mass is evident even taking account of the scatters. The scatter looks very small on the side of high halo mass.

To test the convergence and stability of the results of Fig. 7, we 1.) calculate F_b within radius $2r_{200}$; 2.) analysis 256^3 samples (§3). For the 256^3 samples, we only calculate the F_b within radius $2r_{200}$ to avoid large system error, as r_{200} is under the grid size at the low mass end. The results are given in Fig. 8, in which the halos are identified by the HOP algorithm. It shows that F_b in $2r_{200}$ is about the same as that of r_{200} within the error bars for halos larger than times of $10^{11}\ h^{-1}\ M_\odot$. For halos with mass $\leq 10^{11}\ h^{-1}\ M_\odot$, F_b in r_{200} shows a little lower than that of $2r_{200}$. This result seems to be reasonable, if noted that the baryon fraction of cluster increases with radii (e.g. Ettori & Fabian 1999, Wu & Xue 2000).

For the 256^3 simulation, F_b in radius $2r_{200}$ shows about 10% lower than its counterpart of the 512^3 simulation at halo mass $10^{12} - 10^{11}\ h^{-1}\ M_\odot$. This difference probably comes from the uncertainty caused by the size of grids. The uncertainty of F_b caused by the resolution of 512^3 simulation should be around 10% at halo mass $10^{11}\ h^{-1}\ M_\odot$

Figure 9. compares the baryon fraction as a function of halo mass M_{200} at redshifts $z = 1$, and 2. The halos in Figure 9 are identified by HOP method, which yields similar results as the FOF method. Clearly, it shows the scatter in F_b becomes more significant at lower redshifts, data points have $F_b < 0.2$ at $z = 2$ are quite few, but significantly increases at $z = 1$.

The redshift evolution of F_b is parallel to the IGM turbulence (Zhu et al 2010). The turbulence is fully developed on scales from 0.2 h^{-1} Mpc up to a couple of Mpc since redshift $z \sim 2$. In the IGM density distribution shown in Figure 1, there are about 7.6% of volume with $(1/2)\omega^2 - S_{ij}S_{ij} > 0$ at redshift $z = 0$, while it is merely 2.6% at redshift $z = 2$. The effect of turbulence becomes stronger to slow down the IGM clustering at lower redshifts.

5.3 Comparison with observation

Many measurements on the baryon fraction of galaxies, groups and clusters have been done in recent years. Although it is widely accepted that the baryon missing occurs in gravitational bound objects, the result has not well quantitatively settled yet. For instance, some measurements claim that the baryon fraction in most massive, relaxed galaxy clusters is close to the cosmic mean (e.g. Vikhlinin et al. 2006; Allen et al. 2008), while someone else argues that the baryon fraction of clusters with mass $\sim 10^{14}$ M$_\odot$ is less than the cosmic mean (Giodini et al. 2009). Nevertheless, observation shows that the baryon fraction of objects with mass $\leq 10^{13}$ M$_\odot$ is systematically decreasing with decreasing masses. For galaxy groups and galaxies, the baryon fraction is probably not higher than about 0.1 of the cosmic mean (e.g. Sun et al. 2009; Hoekstra et al. 2005; Heymans et al. 2006; Mandelbaum et al. 2006; Gavazzi et al. 2007).

Figure 10 shows the mass dependence of baryon fraction F_b measured at r_{500} (MaGaugh et al. 2010) and r_{200} (Dai et al (2010). These two data show some difference at mass $\geq 10^{13}\ h^{-1}\ M_\odot$. It is probably due to the cool gas is underestimated with X-ray measurement. It may be also partially caused by the difference in redshifts of the two sample sets.

The result of MaGaugh et al.(2010) can not be fitted by a single power law, but show two-phase feature. In the mass range $> 10^{13}\ h^{-1}\ M_\odot$, $F_b \sim 0.85$, almost independent of object mass. In the mass range $< 10^{13}\ h^{-1}\ M_\odot$, the baryon fraction decreases significantly with the halo mass. F_b is only about 10% of $f_b^{\rm cosmic}$ at $10^{11}\ h^{-1}\ M_\odot$ and further downs to 6% at halo mass of 3×10^{10} $h^{-1}\ M_\odot$.

In Figure 10, we also plot the mean and variance of simulation baryon fraction F_b in r_{200} for HOP halos at z=0. The simulated mass-dependence of F_b shows the similar trend as observation. In the mass range of $\sim 2 \times 10^{11} - 10^{13}$ h^{-1} M$_\odot$, simulation results

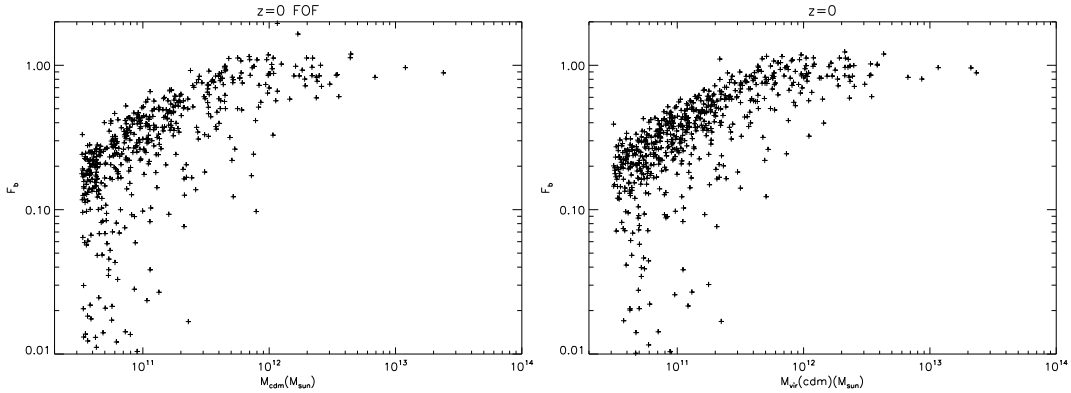

Figure 7. Baryon fraction F_b as function of halo mass M_{200} at $z = 0$. The halos are identified with FOF method (left) and HOP method (right).

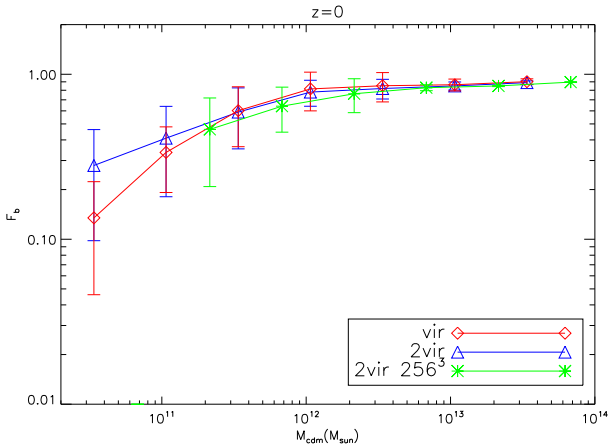

Figure 8. Baryon fraction F_b as function of halo mass M_{200}. The F_b is calculated within the radius r_{200} (red), $2r_{200}$ (blue) for 512^3 samples and within $2r_{200}$ for the 256^3 samples, respectively. The error bars are the rms of the scattered distribution.

are higher than observed data by a factor of about 2, but within the error bars of observed data. The effect of IGM turbulence is not the only reason leading to the baryon missing. Yet it should be an important dynamical reason of the baryon missing, especially for halos with mass $\leq 2 \times 10^{11}\ h^{-1}\ \mathrm{M}_{\odot}$.

6 DISCUSSION

6.1 Comparison with previously numerical studies

The baryon depletion has attracted many studies with cosmological hydrodynamical simulation. As revealed in this paper, the missing baryon could be caused by the IGM turbulence. In order to accurately study the effect of the turbulent IGM on baryon fraction distribution and hence the baryon mission , the algorithm of hydrodynamical simulation should be effective to capture curved shocks, vortices, and intermittence of turbulence in the IGM.

It has been shown that the smoothed particle hydrodynamics (SPH) method may not be able to handle shocks or discontinuities as well as grid method, because the nature of SPH is to smooth between particles(Tasker et al. 2008). The SPH method is found to have strong damping of velocity fluctuations and fluid shear instabilities with respect to grid method (Agertz et al. 2007). Moreover, the artificial viscous force (dissipation) in SPH algorithm will reduce the Reynolds number, and suppress the effect of turbulence (Dolag et al. 2005). These factors would be part of the reasons that some SPH simulations find the baryon fraction in halos to be generally only 10% lower than the cosmic mean(e.g. Eke, Navarro & Frenk 1998; Frenk et al. 1999; Ettori 2006; Crain et al. 2007), where the lower in f_b results from energy transfer during shock formation(Navarro & White 1993).

The Eulerian grid method, including both fixed grid and those with adaptive mesh refinement(AMR), are shown to be effective to pick up the turbulent behavior of baryon fluid in and around galaxies and clusters (e.g. Norman & Bryan 1999; Ryu et al 2008; Molnar et al 2009; Vazza et al. 2009; Burns, Skillman& O'Shea 2010; Ruszkowsky & Oh 2010). However, very few Eulerian simulation has been conducted on the turbulent behavior of IGM other than Zhu et al.(2010). OShea et al. (2005) investigated the baryon fraction in halos at z = 3 during their study on the performance comparison of ENZO and SPH method without looking into tur- bulence. However, their small box, merely 3 Mpc, and relative poorly resolved dark matter halos, typically tens to hundreds parti- cle in a halo, makes a meaningful comparison between their results and those presented in this paper unavailable. The energy cascade would be suppressed in small box, which would significantly restrain the development of turbulence in the IGM. Very recently, the turbulence of IGM is studied with grid based AMR code ENZO including a subgrid scale model for small scale unresolved turbulence in Iapichino et al. (2011), which yields many results similar to Zhu et al (2010). However, statistical study on the baryon fraction is not carried out.

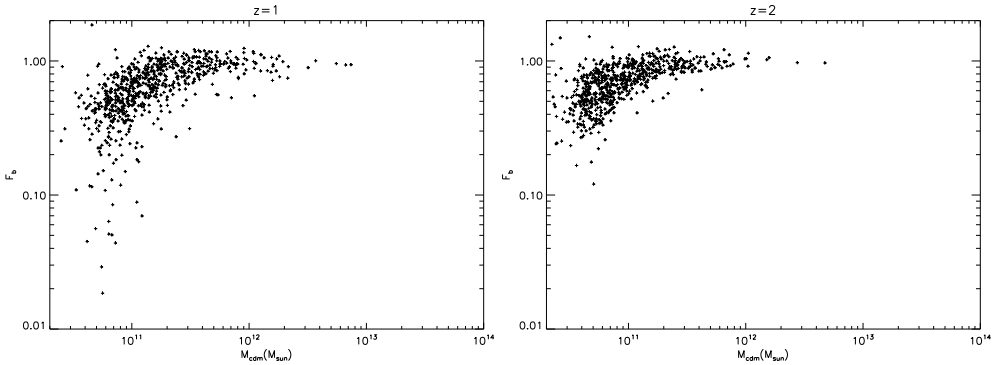

Figure 9. Baryon fraction at $2r_{200}$ vs. halo mass M_{200} at $z = 1$(left) and $z = 2$(right). The halos are identified with HOP method.

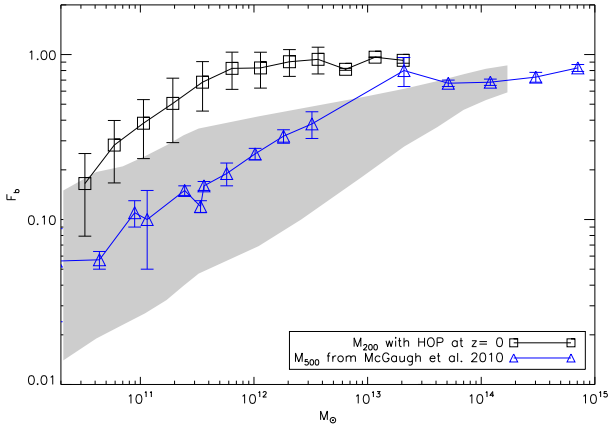

Figure 10. Baryon fraction vs. mass of objects given by the data of McGaugh et al. (2010) (blue); Dai et al (2010) (grey region), and simulation result of f_b at r_{200} of the HOP halos at z=0 with a bin of 0.25 dex in mass.

The WENO algorithm embeded in our simulation uses a convex combination of all the stencils in the reconstruction procedure, where each stencil is assigned with a nonlinear weight depending on the local smoothness. This algorithm provides a high order accurate way to capture the non-oscillatory property near strong discontinuities as well as complex smooth solution features. This feature makes the WENO scheme has gained rapid popularity in the simulation of complex-structure of hydrodynamical field (Shu 1999, 2009). The 5-th order WENO scheme used in this work makes it possible to follow high Reynolds number baryonic fluid. On the other hand, like other high order non-artificial-viscosity scheme, e.g. piecewise perturbation method (PPM), with fixed grid, the computation time needed is much more than the SPH and AMR method, which would become more obvious in higher resolution work.

6.2 Systematic effects

To estimate the effect of turbulence of IGM, a key factor is the upper scale of fully developed turbulence. In some algorithm, the energy of the turbulence is calculated with the fluctuations of velocity with respect to the mean velocity in cells with selected size. An underestimated cell size generally leads to undervalued turbulence (Dolag et al. 2005). In our algorithm the upper scale of turbulence is determined by the relation $P_{\rm vor}(k) = k^2 P_v(k)$, by which the ambiguity in selecting the cell size is avoided.

Star formation and its feedback on the IGM evolution are not considered in our simulation. The injection of hot gas and energy by supernova explosions, AGN or other sources of cosmic rays is not followed. These factors can be properly added, if the star formation history and radiative transfer is well known, which in turn need very high resolution. As mentioned above, the influence of injecting hot gas and energy by supernovae is believed to yield further decrease of F_b in less massive halos, while feedback from AGN might works in massive central galaxies. Including all these mechanisms would give better consistency with observation. Meanwhile, an accurate and robust observation result of baryon fraction in objects from as massive as galaxy cluster to low mass dwarf galaxy is full of challenge. Large scatter in the observed quantities and significant system bias comes from the models applied in object structure and radiative transfer urges much more efforts to deal with.

The spatial resolution of our simulation is $48.8h^{-1}$kpc, which is not enough to simulate virialized halos with mass less than times of $2 \times 10^{10}\ h^{-1}\ {\rm M}_\odot$. The lower limit of the inertial range of turbulence may be affected by the grid resolution, which is already seen in the vorticity power spectra given by samples with different resolution in Zhu et al. (2010). On the other hand, the box size of our simulation is $25h^{-1}$Mpc. It may lose the effect of long wavelength perturbations and hence underestimate the nonlinear evolution of IGM velocity field. Nevertheless, we believe that the basic dynamical picture features revealed by the current samples would be valid when these factors are improved.

7 CONCLUSION

Since gravity is of scale free, it is generally believed that in the scenario of hierarchical clustering, the formation and evolution of halos is scale free in a large range of halo mass. However, the dynamics of the system consisting of two components, dark matter and IGM, is very different from those of one component system. In the nonlinear regime, the hydrodynamical nature of the IGM leads to the dynamical and statistical departure of the IGM from the dark matter. The two component system is no longer to follow the scaling of gravitational clustering of pure dark matter. This deviation is a reason of the baryon missing in gravitational collapsed halos.

The dynamical equation of vorticity does not contain terms of gravity. Therefore, the IGM turbulence characterized by the vorticity will yield, at least, two scales, which violate the scale free of the gravitational hierarchical clustering: 1.) the length scale on which the IGM fluid has been developed to the state of fully developed turbulence; 2.) the mass scale on which the turbulence pressure is comparable with gravity of halo considered. These scales play important role in the evolution of baryon fraction. With cosmological hydrodynamic simulation, we find that at $z = 0$ the first scale is about 3 h^{-1} Mpc, and the second one is $\sim 10^{11}$ h^{-1} $\mathrm{M}_{\odot}$. With these results, we reach to the following conclusions:

i. The distribution of baryon fraction is highly nonuniform on scales from hundreds kpc to a few of Mpc, and f_b varies from as low as 1% to a few times of the cosmic mean.

i. The turbulence can effectively prevent the IGM from falling into potential wells of dark matter halos with mass $\sim 10^{11}$ h^{-1} $\mathrm{M}_{\odot}$.

iii. The f_b in dark matter halos is decreasing from $0.8 f_b^{\mathrm{cosmic}}$ at halo mass scales around 10^{12} h^{-1} $\mathrm{M}_{\odot}$ to $0.3 f_b^{\mathrm{cosmic}}$ at 10^{11} h^{-1} $\mathrm{M}_{\odot}$ due to the turbulent state of the IGM.

The estimated turbulence pressure at $z = 0$ correspond to a random motion with r.m.s velocity of about $50 - 100$ km s^{-1} in the scale range from hundreds of kpc and up to ~ 2 Mpc. The turbulent pressure is dynamical and non-thermal. When the turbulence dissipated, its kinetic energy becomes the thermal energy. It yields the entropy in halos (He, Feng, & Fang 2005). Therefore, the dissipation of turbulence actually is a mechanism of heating, which gives a compensation to the cooling of gas in halos. This result is consistent with the Burgers' shock heating (He et al 2004). In summmary, the dynamics of turbulence can effectively affect the baryon fraction of halos .

8 ACKNOWLEDGMENTS

WSZ acknowledges the support of the International Center for Relativistic Center Network (ICRAnet). Our work takes advantage of open facilities provided by the NASA HPCC ESS group at the University of Washington (http://www-hpcc.astro.washington.edu/). This work is partially supported by the National Science Foundation of China grant NSFC 10633040, 10725314 , 10621303 and the 973 Program under contract No. 2007CB815402.

REFERENCES

Agertz O., et al., 2007, MNRAS, 380, 963
Allen, S. W., Rapetti, D. A., Schmidt, R. W., Ebeling, H., Morris, R. G., & Fabian, A. C., 2008, MNRAS, 383, 879
Anderson, M. E., & Bregman J. N., 2010, ApJ, 714, 320
Batchelor, G.K. 1959, *The Theory of Homogeneous Turbulence*, (Canbridge University Press)
Batchelor, G.K. 2000, *An Introductrion to fluid Dynamics*, (Canbridge University Press)
Berera, A., & Fang, L. Z., 1994, Phys. Rev. Lett., 72, 458
Benson A. J., Lacey C. G., Baugh C. M., Cole S., Frenk C. S., 2002, MNRAS, 333, 156
Benson A. J., Bower R. G., Frenk C. S., Laccy C. G., Baugh C. M., Cole S., 2003, ApJ, 599, 38
Boldyrev, Linde, T. & Polyakov, A., 2004, Phs. Rev. Lett. 93, 184503
Bonazzola, S., Falgarone, Heyvaerts, J., Perault, M. & Puget, J. 1987, A&A, 172, 293
Burns, J., Skillman, S.,& O'Shea, B., 2010, ApJ, 721, 1105
Carrillo, J. A., Gamba, I. M., Majorana, A., & Shu, C. W. 2003, J. Comput. Phys., 184, 498
Chandrasekhar, S. 1951a, Proc. Roy. Soc. A210, 18
Chandrasekhar, S. 1951b, Proc. Roy. Soc. A210, 26
Crain. R. A., Eke V. R., Frenk C. S., Jenkins A., McCarthy I. G., Navarro J. F., & Pearce F. R., 2007, MNRAS, 377, 41
Croton D. J., Springel V., White S. D. M., De Lucia G., Frenk C. S., Gao L., Jenkins A., Kauffmann G., Navarro J. F., & Yoshida N., 2006, MNRAS, 365, 11
Dai, X. Y., Bregman, J. N., Kochanek, C. S., & Rasia, E., 2009, ApJ, 719, 119
de Silva, A,C., Kay, S.T., Lidde, A. R. & Thomas, P. A. 2004, MNRAS, 348, 1401
Dekel A., Silk J., 1986, ApJ, 303, 39
Dolag, K., Vazza, F., Brunetti G., & Tormen G. 2005, MNRAS, 364, 753
Dunkley, J. et al., 2009, ApJS, 180, 306
Eisenstein, D. J., & Hut, P. 1998, ApJ, 498, 137
Eke V. R., Navarroo J. F., Frenk C.S., 1998, ApJ, 503,569
Emanuel, G. 2000, Analytical Fluid Dynamics, 2nd ed. CRC press
Ettori. S. 2003, MNRAS, 344, L13
Ettori, S., Dolag, k., Borgani, S., Murante, G., 2006, MNRAS, 365,1021
Ettori, S. & Fabian, A. C. 1999, MNRAS, 305, 834
Fang, L. Z. & Zhu, W.S., 2011, Advances in Astronomy, 2011, Artcle ID 492480
Feng, L.L., Shu, C.-W., & Zhang, M.P. 2004, ApJ, 612, 1
Frenk C. S. et al., 1999, ApJ, 525, 554
Gavazzi, R., Treu, T., et al., 2007, ApJ, 667, 176
Gnedin N. Y., 2000, ApJ, 542, 535
Giodini, S., et al. 2009, ApJ 703, 982
Grasso, F., & Pirzzoli, R., 2000a, Physics of Fluids, 12, 3265
Grasso, F., & Pirzzoli, R., 2000b, Theor. and Comp. Fluid Dyn.,13, 421
Gurbatov, S. N., Saichev, A. I., & Shandarin, S. F., 1989, MNRAS, 236, 385
Kauffmann G., Colberg J. M., Diaferio A., White S. D. M., 1999, MNRAS, 303, 188
He, P., Feng, L. L., & Fang, L. Z., 2004, ApJ, 612, 14
He, P., Feng, L.L., & Fang, L.Z. 2005, ApJ, 623, 601
He, P., Liu, J., Feng, L.L., Shu, C.-W., & Fang, L.Z. 2006, Phys. Rev. Lett, 96, 051302
Heymans, C., Bell, E. F. et al., 2006, MNRAS, 371, L60
Hoekstra, H., Hsieh, B. C., Yee, H. K. C., Lin, H., & Gladders, M. D. 2005, ApJ, 635, 73
Hoeft M., Yepes G., Gottlober S., Springel V., 2006, MNRAS, 371,401
Iapichino, L., Schmidt, W., Niemeyer, J. C., & Merklein J. 2011, ariv:1102.3352
Jiang, G. & Wu, C.C. 1999, J. of Comput. Phys., 150, 561-594.
Jones, B. T. 1999, MNRAS, 307,376
Kang, H. S., Ryu, D. S., Cen, R. Y., & Ostriker, J. P., 2007, ApJ, 669, 729
Keres, D., Katz, N., Dave, R., Fardal, M., & Weinberg, David H., 2009, MNRAS, 396, 2332
Kim, B., He, P., Pando, J., Feng, L. L. & Fang, L. Z. 2005, ApJ, 625, 599
Komatsu, E., et al. 2009, ApJS, 180, 330
Lagha, M., Zhong, X. L., Eldredge, J., & Kim, J., 2009, AIAA 2009-1136
Landau, L., & Lifshitz, E. 1987, Fluid Mechanics, 2ed Edition(Pergamon Press)
Lässig, M. 2000, Phys. Rev. Lett., 84, 2618

Lin, C. C., 1966, Theory of Hydrodynamical Stability (Cambridge University)
Liu, J.R., & Fang, L.Z. 2008, ApJ, 672, 11
Liu, J.R., Jamkhedkar, P., Zheng, W., Feng, L. L., & Fang, L. Z. 2006, ApJ, 645, 861
Lo, S.-C., Blaisdelly, G. A. & Lyrintzisz, A. S., 2007, AIAA 2007-827
Lu, Y., Chu, Y.Q., & Fang, L.Z. 2009, ApJ, 691, 43
Lu, Y., Zhu, W. S., Chu, Y.Q., Feng, L. L.& Fang, L.Z. 2010, MNRAS, 408, 452
Mac Low M.-M., Ferrara A., 1999, ApJ, 513, 142
Matarrese, S., & Mohayaee, R. 2002, MNRAS, 329, 37
Martin, M.P., Piomelli, U., & Candler, G.V. 2000. Theor. and Comp. Fluid Dyn. 13, 361-376
McGaugh, S. S., Schombert, J. M., de Blok, W. J. G., & Zagursky, M. J., 2010, ApJ, 708, L14
Mandelbaum, R., Seljak, U., Cool, R. J.. Blanton, M., Hirata, C. M.. & Brinkmann, J., 2006, MNRAS, 372, 758
Mo H. J., Yang X., van den Bosch F. C., Katz N., 2005, MNRAS, 363, 1155
Molnar, S.M., Hearn, N., Haiman, Z., Bryan, G., Evrard, A. E. & Lake, G., 2009, ApJ, 696, 1640
Navarro J. F., White S. D. M., 1993, MNRAS, 265, 271
Norman, M., & Bryan, G., 1999, LNP, 530, 106
O'Shea, B. W., Nagamine, K., Springel, V., Hernquist, L. & Norman, M.L., 2005, ApJS, 160, 1
Pando, J., Feng, L. L., & Fang, L. Z. 2004, ApJS, 154, 475
Pfrommer, C., Springel, V., Enblin, T. A., & Jubelgas, M. 2006, MNRAS, 367, 113
Pichon, C. & Bernardeau, F. 1999 A&A 343, 663
Picone, J.P., Oran, E.S., Boris, J.P. & Young Jr, T.R. 1984, NRL Memorandum Report A234441
Pirozzoll, S., 2002, Journal of Computational Physics, 178, 81
Polyakov, A. M. 1995, Phys. Rev., 52, 6183
Pueblas & Scoccimarro 2008 Phys. Rev. D, 80, 043504
Rehman, S. F., Eldredge, J. D., Zhong, X. L., & Kim, J., 2009, AIAA, 2009-941
Ruszkowski, M., & Oh, S. P. 2010, ApJ, 713, 1332
Ryu, D. S., Kang, H. S., Hallman, E., & Jones, T. W., 2003, ApJ, 593, 599
Ryu, D., Kang, H., Cho, J., & Das, S. 2008, Science, 320, 909
Shandarin, S. F., & Zeldovich, Y. B., 1989, RvMP, 61, 185
Shu, F. H., 1992, The Physics of Astrophysics Volume II: Gas Dynamics(University Science Books)
Shu, C.-W, 1999, in Lecture Notes in Computational Science and Engineering, 9, 439
Shu, C.-W, 2009, SIAM Review, 51, 82
Somerville, R. S., Hopkins, P. F., Cox, T. J., Robertson, B. E., & Hernquist, L., 2008, MNRAS, 391, 481
Sun, M., Voit, G. M., Donahue, M., Jones, C., Forman, W., & Vikhlinin, A., 2009, ApJ, 693, 1142
Tasker, E. J. et al., 2008, MNRAS, 390, 1267
Theuns, T., Leonard, A., Efstathiou, G. ,Pearce, F. R., & Thomas, P. A. 1998, MNRAS, 301, 478
Tozzi, P., & Norman, C. 2001, ApJ, 546, 63
Valageas, P., & Silk, J. 1999, A&A, 350, 725
Vazza, F., Brunetti, G., Kritsuk, A., Wagner, R., Gheller, C., & Norman, M. 2009, A&A, 504, 33
Vergassola, M., Dubrulle, B., Frisch, U., & Noullez, A. 1994, A&A, 289, 325
Visbal, M. R., & Gaitonde, D. V., 2005, AIAA 2005-1265
Vikhlinin, A., Kravtsov, A., Forman, W., Jones, C., Markevitch, M., Murray, S. S., & Van Speybroeck L., 2006, ApJ, 640, 691
Voit, G. M. Bryan, G. L., Balogh, M. L., & Bower, R. G. 2002, ApJ, 576, 601
White, S. D. M., Frenk, C. S., 1991, ApJ, 379, 52
Wu, X.P. & Xue, Y.J. 2000, MNRAS, 311, 825
Xue, Y. J. & Wu, X. P. 2003, ApJ, 584, 34
Yuan, Q., Wan H. Y., Zhang T. J., Liu J. R., Feng L. L., & Fang L. Z. 2009, NewA, 14, 152
Zhang, P. J., & Pen, U. L. 2003, ApJ, 588, 704
Zhang, Y. T., Shi, J., Shu, C. W., & Zhou, Y., 2003, Phys. Rev. E, 68, 046709
Zhang, T. J., et al. 2006, ApJ, 642, 625
Zheng, W., et al. 2004, ApJ, 605, 631
Zhu, W. S., Feng, L. L., & Fang, L. Z., 2010, ApJ, 712, 1

APPENDIX A: SHOCK CAPTURING ALGORITHM OF WENO SCHEME

In the WENO scheme, the smoothness of a hydrodynamical quantities $U = (\rho, p, v, E)$ in any dimension is measured by

$$\eta_i = \frac{1}{4}(U_{i+1} - U_{i-1})^2 + \frac{13}{12}(U_{i+1} - 2U_i + U_{i-1})^2, \qquad \text{(A1)}$$

where the definition of U_i is the same as that given in the Appendix of Zhu et al (2010).

With η_i, we can construct the one-dimensional discontinuous detector by

$$DDF_i = \left| \frac{(\eta_i)^{1/2}}{U_{i+1} + 2U_i + U_{i-1}} \right|^n . \qquad \text{(A2)}$$

where $n = 1, 2, ...$ We use $U = p$ and $n = 2$ to detect the discontinuous surface (Visbal & Gaitonde 2005; Lo et al. 2007). For each cell, we calculate DDF_i in three directions. The value of DDF is normalized by the max of DDF among all the cells. Then, a threshold parameter of 1.0^{-4} of DDF_i is used to flag discontinuous zone with $DDF_i > 10^{-4}$. Finally, we pick up the shocks with Mach number $M_a > 1.5$ from the flagged cells by checking the conditions as that given by Ryu et al. 2003.